


Realization of inverse-designed underwater acoustic superscattering

Di Wang,¹ He Gao^{1,2}, Zhongming Gu^{1,*}, Yinjie Su,¹ Jiamin Guo,¹ Chen Liu,¹ Zhongqing Su^{1,2}, and Jie Zhu^{1,†}

¹*Institute of Acoustics, School of Physics Science and Engineering, Tongji University, Shanghai 200092, People's Republic of China*

²*Department of Mechanical Engineering, The Hong Kong Polytechnic University, Kowloon, Hong Kong SAR, People's Republic of China*

 (Received 6 February 2024; revised 18 April 2024; accepted 3 May 2024; published 6 June 2024)

Superscattering is a unique wave phenomenon that allows subwavelength objects to produce a large scattering cross section, surpassing the fundamental single-channel limit. This effect has been extensively studied in many wave systems, such as electromagnetic waves, water surface waves, and airborne acoustics. However, in the context of underwater acoustics, achieving superscattering with a single material has remained unexplored due to complex acoustic-solid interactions. Here, we have inversely designed a simple yet efficient structure to achieve the superscattering of ultrasound in water. Both numerical simulations and experimental results show that the proposed superscatterer exhibits significantly stronger ultrasound backscattering compared with a bare rigid cylinder. Furthermore, we construct a superscattering chain barrier. It is able to enhance ultrasound insulation while maintaining water permeability. This chain barrier is demonstrated to be robust for ultrasound with a wide range of incident angles. The results from this study are expected to benefit various fields of underwater acoustics, particularly in marine detection and sea-life protection.

DOI: [10.1103/PhysRevApplied.21.064011](https://doi.org/10.1103/PhysRevApplied.21.064011)

I. INTRODUCTION

Intriguing wave phenomena enabled by acoustic metamaterials [1–4] have gained significant attention due to their potential to revolutionize diverse fields of acoustic engineering, such as superresolution imaging [5–7], acoustic cloaking [8–11], and acoustic enhanced focusing [12–15]. As important wave behavior, acoustic superscattering [16–18] is a fascinating phenomenon due to its ability to enhance wave-matter interactions, opening up possibilities for energy harvesting [19], sound insulation [20], and acoustic sensing [21]. Typically, it is widely believed that the scattering effect is primarily influenced by the larger physical scatterer size relative to the wavelength of interest. Recent studies show that, with decorated structures [16,17,20,22,23] or concentrated coatings [18,24–28], enhanced scattering of the subwavelength scatterer can be obtained. By combining multiple resonances [29–34], it is possible to greatly enhance the scattering cross section (SCS), surpassing the limits imposed by the signal channel limit in two-dimensional [27] and three-dimensional (3D) space [28], leading to a more pronounced scattering effect. Although the concept

of superscattering was theoretically and experimentally demonstrated in electromagnetics [24], optics [23,35], water surface waves [25], and airborne acoustics [16,17], it remains to a big challenge to design an underwater superscatterer, owing to the complex acoustic-solid interactions in underwater acoustics. Very recently, a multilayered cylindrical structure [18], consisting of rubber and acrylic, was numerically proposed to realize acoustic superscattering in water. However, there is a lack of experimental demonstrations of the superscattering effect using easily fabricated structures.

Recent advancements in the application of the genetic algorithm (GA) [36–39] for addressing acoustic wave-matter interactions underwater have shown promising results, circumventing the challenges in deriving the analytical solutions. Furthermore, by combining the GA with the finite-element method, complete information on the acoustic fields in both fluid and solid domains can be obtained; this is then utilized in the optimization algorithm to find the optimal solution. This approach has facilitated the realization of several impressive acoustic devices [37,39–41] in water by leveraging the GA to optimize subwavelength structures, thus showing its significant potential in designing intriguing wave manipulations.

Here, we present an effective approach to design an acoustic superscatterer (SS) decorated with finlike

*Corresponding author: zhmgu@tongji.edu.cn

†Corresponding author: jiezhu@tongji.edu.cn

structures, which greatly enhance the sound-scattering performance in water. Here, finlike structures are employed to enrich the resonant modes to break the single-channel limit by utilizing the acoustic-solid interaction. The structural parameters of the decorations are optimized globally to obtain maximum SCS via the GA. Hence, the scattered field of the SS has a much larger ultrasound shadow region compared with that of a cylindrical scatterer (CS) with the same diameter. Additionally, we have arranged multiple SSs in a chain configuration, creating a permeable barrier that effectively blocks the ultrasound waves while allowing water flow between the scatterers. This permeable barrier demonstrates strong ultrasound insulation across a wide range of incident angles. This excellent sound-insulation ability helps to promote the development of noise reduction underwater. In addition, the structure obtained by the reverse design is flexible and adjustable, according to different operating frequencies. Thus, we anticipate that our design holds potential for application in many fields, such as medical imaging, underwater detection, and sea-life protection.

II. REALIZATION AND VALIDATION OF SUPERSCATTERING

First, we consider the scenario where a subwavelength CS is immersed in water. When the ultrasound wave impinges on it, the scattering effect is weak, and the wave propagates with little distortion, as depicted in Fig. 1(a). On the contrary, as Fig. 1(b) illustrates, superscattering can offer a dramatically enhanced scattered ultrasound field, even though the size of the SS is smaller than a wavelength. Figures 1(c) and 1(d) show the geometric configurations of the CS and SS, respectively. Both scatterers have identical radii, $r = 3$ mm, and heights, $H = 50$ mm. Here, only the in-plane acoustic field is considered in the following simulations and experiments. The finlike structures are decorated periodically around the SS and contain two adjustable variables: the length, h , and the spacing, w , between adjacent units, which are the inputs of the optimization algorithm. With the change of geometric parameters, the vibrational displacement of the scatterer changes correspondingly under the action of the incident acoustic wave, and stronger resonant modes can be excited. See Appendix A for a more detailed discussion.

The GA combined with the finite-element method is adopted to optimize the appropriate frequency, f_i , and geometrical parameters: the spacing, w_i , and the length, h_i ($i = 1, 2 \dots N$) (i denotes the i th iteration), which all act as the degrees of freedom for optimization. Considering the material properties and the limits of the fabrication method (3D metal printing), we set the initial values for structural parameters and specify the range of optimization variables. They are continuously optimized to minimize

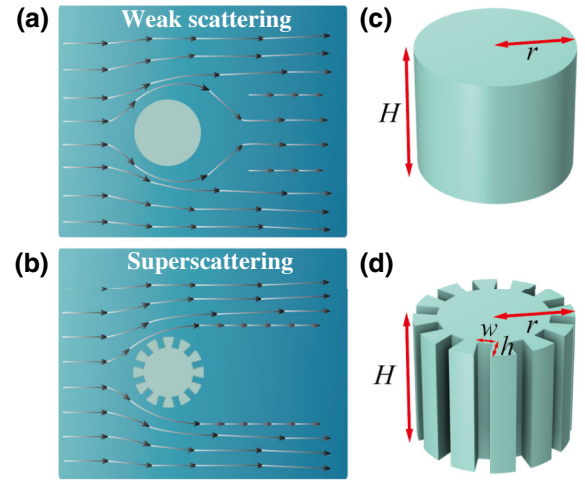


FIG. 1. Conceptual schematic of the superscattering effect. (a),(b) Power-flow distribution around the CS and the SS with the plane ultrasound wave incident from the left. Arrows illustrate the Poynting vectors. (c),(d) Models of the CS and the SS. Radius and height for both CS and SS cells are r and H , respectively. SS is composed of 12 finlike decorations placed circularly. Geometrical parameters w and h for SS are optimization variables, representing the spacing and length of the finlike structures.

the target function described as

$$T = \frac{1}{N} \sum_i^N |p_{i}|^2 (i = 1, 2 \dots N), \quad (1)$$

where p_{i} is the total acoustic pressure at a discrete point and N is the total number of discrete points in the target region. After generating the primary population, the fitness function in Eq. (1) is calculated by retrieving information about the ultrasound field via the finite-element method (COMSOL Multiphysics). Then, we judge whether the fitness score has converged to a critical value with repeated iterative calculations. The detailed optimization convergence process is shown in Appendix B. When the optimization process ends, the best-fit values for the target variables would be the output, and then the optimal structure at the fixed frequency can be obtained [42].

After optimization, the structural parameters are finally fixed as $w = 0.6$ mm and $h = 0.9$ mm. The scattering performance of this configuration can be verified in the full-wave simulations. In the simulations, the background medium is selected to be water with a density and sound speed of 998 kg/m^3 and 1480 m/s , respectively. The sample is made of stainless-steel metal with a density, Poisson's ratio, and Young's modulus of 7850 kg/m^3 , 0.3 , and 200 GPa , respectively. The impedance mismatch between steel and water is far less than that in air, which means that the acoustic-solid interaction cannot be ignored. Figures 2(a) and 2(b) show the simulated acoustic pressure fields when a plane ultrasound wave illuminates the SS and CS, respectively, at a frequency of 210 kHz . As demonstrated

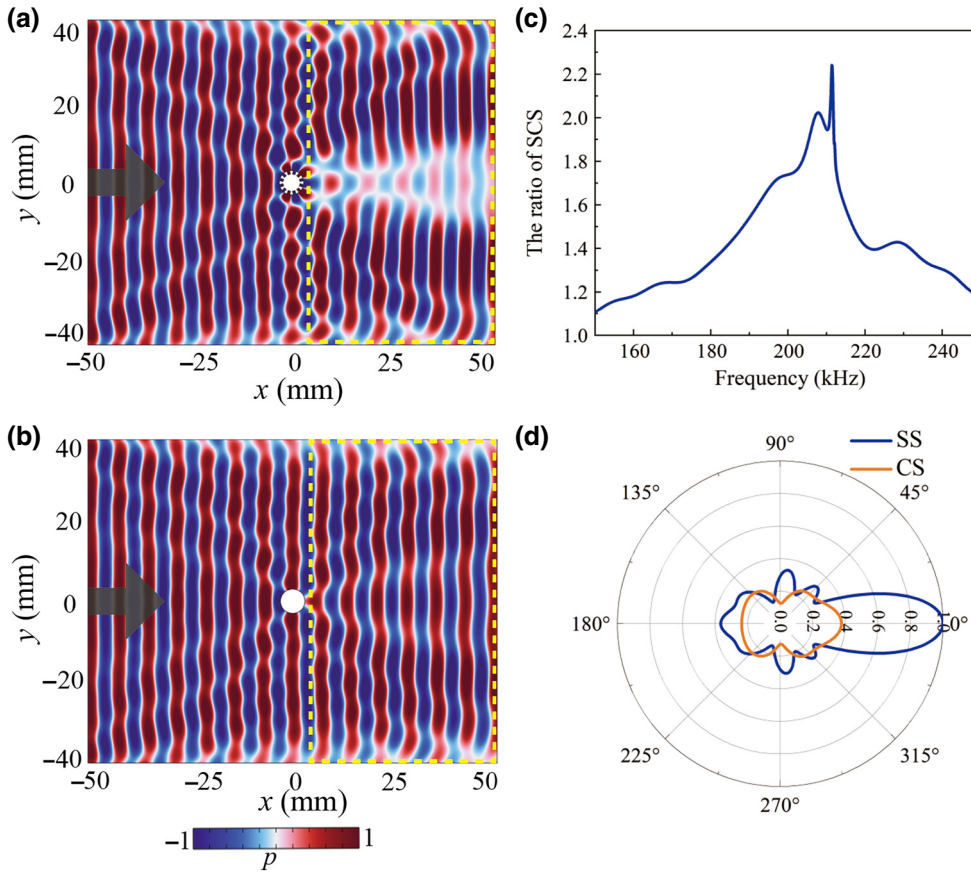


FIG. 2. Numerical simulations. (a),(b) Simulated acoustic fields for SS and CS, respectively. (c) Ratio of scattering cross section between SS and CS for one unit cell. (d) Scattered-energy directionality for SS (blue line) and CS (yellow line).

in Fig. 2(a), the SS causes strong scattering of the incident wave, which leads to an explicit area behind the SS that no wave enters. However, the diffracted propagation at the back of the CS, as shown in Fig. 2(b), indicates a much weaker scattering.

To quantitatively characterize the scattering abilities of the SS and CS, we calculate the total SCS by

$$S_{\text{scs}} = \int_0^{2\pi} \frac{|p_s(\theta)|^2}{|p_i(\theta)|^2} r_0 d\theta, \quad (2)$$

where r_0 is the radius of the calculated circle. In this equation, the scattered pressure, $p_s(\theta)$, is determined by the incident pressure, $p_i(\theta)$, and the total pressure, $p_t(\theta)$, i.e., $p_s(\theta) = p_t(\theta) - p_i(\theta)$. They are all obtained from the reference circle with a radius, r_0 , of 30 mm. For a better visualization of the superscattering performance, the ratio of SCS between the SS and CS has been plotted in Fig. 2(c). It clearly shows that the scattering induced by the SS is much stronger than that of the CS around 210 kHz, which is consistent with the simulated results in Figs. 2(a) and 2(b). The superscattering effect can also be observed by the directionality of the scattered waves patterned in Fig. 2(d). The CS sends energy almost uniformly

in all directions, while the SS has obvious and intense backscattering energy.

We conduct experimental verifications to confirm the superscattering phenomenon, and a detailed diagram is available in Appendix C. The stainless-steel samples are fabricated by 3D metal printing with a manufacturing accuracy of 0.1 mm. The whole experiments are conducted in the scanning tank and measured via an automated scanning system. During the measurement, the pulse signal (a five-period 210-kHz sine wave) is first generated by the signal generator (Tektronix, AFG3022C), transfers to the amplifier (T&C, AG Series Amplifier), and is finally emitted by the transducer (DYW-200-NB). The sound field in the target region is probed by the needle hydrophone (Precision Acoustics, NH2000) mounted on a three-dimensional-axis moving stage. The spatial resolution of the measurement is 1 mm. The detected signals are finally sent to the oscilloscope (National Instruments, PXI-5124) for postprocessing by a computer.

To compare the scattering performance, the acoustic pressure fields in the selected regions behind the SS and CS, encircled by yellow dotted boxes in Figs. 2(a) and 2(b), are measured. The experimental results presented in Figs. 3(a) and 3(b) show that a clear shadow region is induced by the SS, while the measured field behind the CS

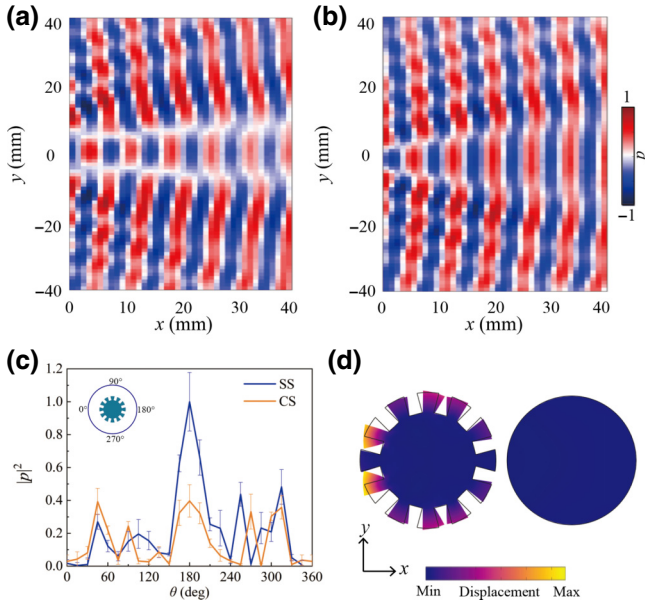


FIG. 3. Experimental demonstrations. (a),(b) Measured acoustic pressure fields for SS and CS, respectively. Measuring areas are denoted by the yellow dotted rectangles in Figs. 2(a) and 2(b), respectively. (c) Scattering-energy profiles varying with θ for SS (blue line) and CS (yellow line) along a reference circle with a radius of 10.5 mm. (d) Simulated total displacement fields of SS and CS at 210 kHz. Colormap and deformation both denote the magnitude of the displacement.

shows an intact wave front. Meanwhile, we also measure the scattering-energy profiles along the reference circle with a radius of 10.5 mm. As presented in Fig. 3(c), the sound wave incident on the SS experiences much stronger backscattering than the CS when θ is around 180° . For a better understanding of the underlying mechanism, we also numerically analyze the vibration modes of the SS and CS. Figure 3(d) shows the total displacement fields with an incident frequency of 210 kHz. It is obvious that, with the optimized finlike structures, the SS can generate much richer resonant modes. The fin tips vibrate forcefully to disrupt the incoming ultrasound.

III. DESIGN AND VALIDATION OF THE SUPERSCATTERING CHAIN BARRIER

To take advantage of the intriguing properties of the SS, we have developed a sparse ultrasound barrier. It consists of an array of SSs along a straight line to achieve high-efficiency sound insulation while also allowing unrestricted water flow. We still adopt the GA and finite-element method combination to select the most suitable period, d , of the array, so that ultrasound insulation can be maximized. Considering the transducer size, we choose to form a nine-unit array to eliminate the barrier's boundary effect. The samples are fabricated with stainless-steel

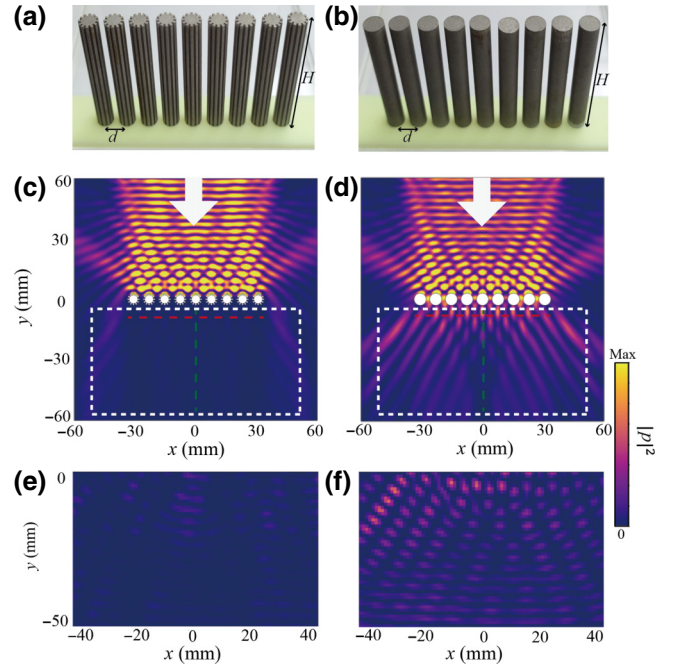


FIG. 4. Ultrasound barrier based on the SS array. (a),(b) Photographs of the 3D-printed SS and CS samples with the same height, $H = 50$ mm, and period, $d = 7.7$ mm. (c),(d) Simulated acoustic energy fields for the SS array and the CS array, respectively. (e),(f) Measured acoustic energy fields for the SS array and the CS array, respectively. Measuring areas are encircled by the white dotted rectangles in (c),(d).

metal. For comparison, an array of CSs in the same arrangement is also investigated, as shown in Figs. 4(a) and 4(b).

We first conduct simulations to examine the performance of the designed barrier. As shown in Figs. 4(c) and 4(d), the optimized SS barrier clearly possesses much stronger sound insulation, compared with the CS barrier. The experiments carried out in water for the two barriers obviously agree well with the corresponding simulations. The measured results, plotted in Figs. 4(e) and 4(f), confirm the strong ultrasound-insulation capability of the SS barrier at the predesigned frequency. It should be noted that the working frequency can be tuned arbitrarily by adjusting the structural parameters.

Due to the isotropic nature of our SS unit, the ultrasound barrier is expected to persist in the superscattering properties for a wide range of incident angles. To prove this hypothesis, we calculate the total acoustic energy along the red and green dotted lines indicated in Figs. 4(c) and 4(d), with different incident angles. As shown in Figs. 5(a) and 5(b), it is evident that the ultrasound within a certain range of incident angles can barely pass through the SS array barrier. We select two specific angles, 10° and 20° , and measure the ultrasound transmission. At these two

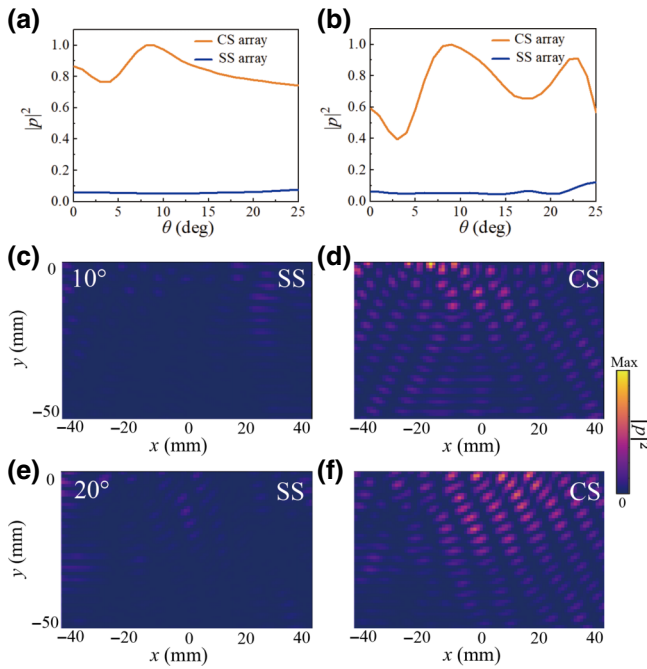


FIG. 5. Robustness of sound insulation towards the incident angle, θ . Total acoustic energy integrated along (a) red and (b) green dashed lines in Figs. 4(c) and 4(d) as a function of incident angle. Measured acoustic energy fields for (c) the SS array and (d) the CS array with an incident angle of 10° . Measured acoustic energy fields for (e) the SS array and (f) the CS array with an incident angle of 20° . Measuring areas are the same as those in Figs. 4(c) and 4(d).

angles, the ultrasound signals transmitted through the SS array barrier are quite limited, as presented in Figs. 5(c) and 5(e). The ultrasound fields that have been normalized to the same value are remarkably weaker than that of the CS array in Figs. 5(d) and 5(f), effectively demonstrating great ultrasound insulation in both cases.

IV. CONCLUSION

To sum up, we have successfully realized ultrasound superscattering in water by introducing finlike decorations to bring additional resonance modes. With the aid of an inverse design approach, the genetic algorithm, and the

finite-element method, we were able to avoid complex analytical calculations and still fully consider the fluid-structure interaction in optimizing the acoustic superscatterer. Furthermore, the proposed scatterer cells were put into a chain configuration. We utilize the coupling of cells' resonance modes to create an effective ultrasound-blocking barrier. The simulation and experimental measurements have shown excellent agreement, confirming our proposed model and the superscattering capability. Our work may benefit potential applications in fields where enhanced scattering is demanded, such as in constructing an acoustic radiation force and medical ultrasound imaging.

Data that support the findings of this study are available from the corresponding author upon reasonable request.

ACKNOWLEDGMENTS

This work was supported by the National Key R&D Program of China (Grant No. 2022YFA1404400), the Research Grants Council of Hong Kong SAR (Grant No. AoE/P-502/20), the National Natural Science Foundation of China (Grants No. 92263208 and 12304494), and the Open Fund of State Key Laboratory of Acoustics (Grant No. SKLA202313).

APPENDIX A: INTERNAL MECHANISM OF THE OPTIMIZATION PROCESS

In this work, the finlike structure is equivalent to the resonator, and during optimization, the geometric parameters of the finlike structure and the frequency gradually reach the best matching relationship, so as to achieve superscattering. In this process, with the incident wave, the vibrational displacement of the optimized structure also increases, which means that more resonance modes are excited, as shown in Fig. 6.

APPENDIX B: SCHEMATIC DIAGRAM OF THE OPTIMIZATION PROCESS

In this work, we try to realize the superscattering of the scatterer, so that the total acoustic energy in the target region behind the scatterer acts as the optimization target.

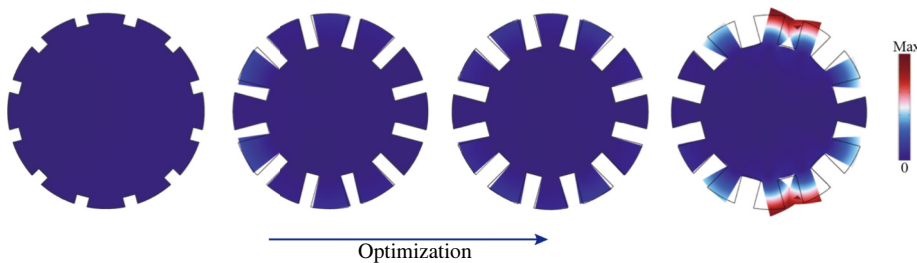


FIG. 6. Change of vibration displacement during optimization.

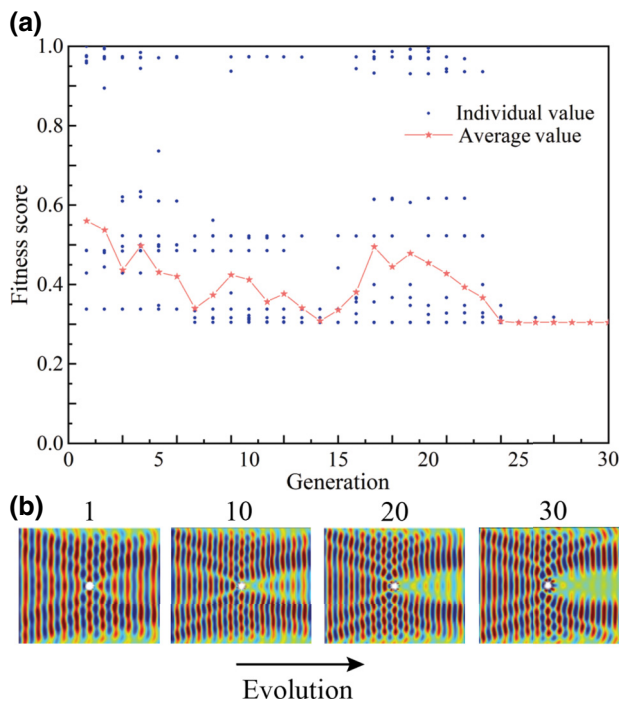


FIG. 7. (a) Fitness score with evolution of the generation. (b) Representative optimization results during evolution.

Generally, a lower integral value indicates a better super-scattering performance, thus the optimization objective is to minimize this fitness score. The generation in the optimization is set to be 30, with each generation consisting

of 26 individuals. The average value of the fitness scores for all 26 individuals is the score for that generation. In Fig. 7(a), we illustrate the optimization process of the GA. The blue dots represent the fitness score of each individual and the line of red stars represents the average value, which demonstrates a decreasing trend in fitness score as the generation increases, eventually reaching a steady value. Additionally, we examine the evolution of the acoustic pressure field, as depicted in Fig. 7(b), which demonstrates a gradual enhancement of the scattered acoustic pressure with an increase in generation.

APPENDIX C: THE EXPERIMENTAL SCHEMATIC DIAGRAM

During the measurement, the signal-emission device (transducer) and the detecting device (hydrophone), along with the sample, are fully submerged in water and positioned on the designed holders, as shown in Fig. 8. The distance between the transducer and the sample is carefully adjusted to ensure that the incident wave illuminating the sample is a plane wave. The selection of the measurement area depends on specific cases. For the single scatterer, a rectangular area of $40 \times 80 \text{ cm}^2$ is selected. When measuring its directivity, a series of discrete points along the reference circle with a radius of 10.5 mm are detected. In the case of verifying sound insulation, the measurement is conducted in a rectangular area of $50 \times 80 \text{ cm}^2$.

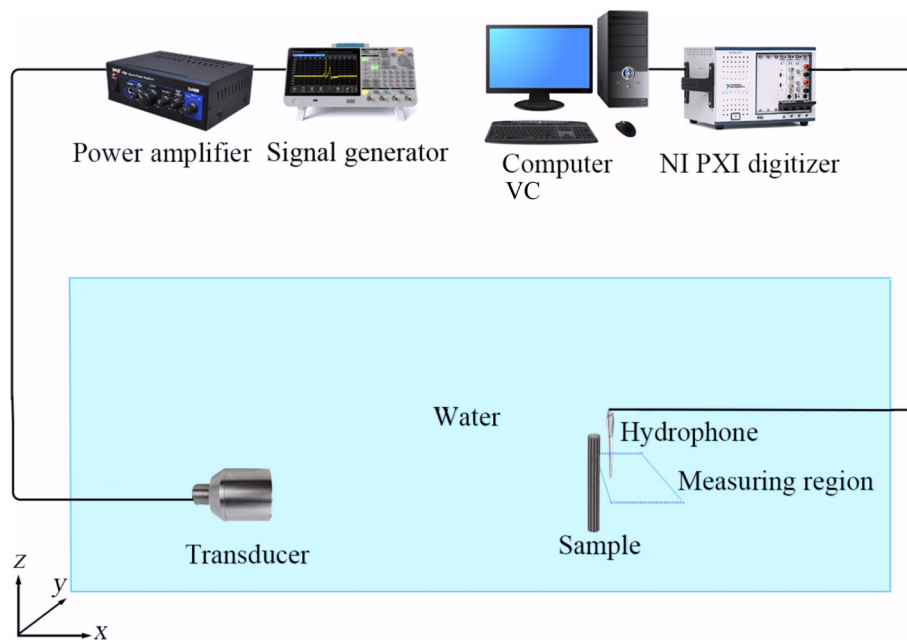


FIG. 8. Diagram of the experimental setup.

- [1] B. Assouar, B. Liang, Y. Wu, Y. Li, J.-C. Cheng, and Y. Jing, Acoustic metasurfaces, *Nat. Rev. Mater.* **3**, 460 (2018).
- [2] A. L. Chen, Y.-S. Wang, Y.-F. Wang, H.-T. Zhou, and S.-M. Yuan, Design of acoustic/elastic phase gradient metasurfaces: Principles, functional elements, tunability, and coding, *Appl. Mech. Rev.* **74**, 020801 (2022).
- [3] S. A. Cummer, J. Christensen, and A. Alù, Controlling sound with acoustic metamaterials, *Nat. Rev. Mater.* **1**, 16001 (2016).
- [4] N. Gao, Z. Zhang, J. Deng, X. Guo, B. Cheng, and H. Hou, Acoustic metamaterials for noise reduction: A review, *Adv. Mater. Technol.* **7**, 2100698 (2022).
- [5] X. Fan, Y. Zhu, N. Li, C. Weng, and B. Assouar, Acoustic metaholograms for encrypted information transmission, *Phys. Rev. Appl.* **20**, 044048 (2023).
- [6] Y. Tian, Q. Wei, Y. Cheng, and X. Liu, Acoustic holography based on composite metasurface with decoupled modulation of phase and amplitude, *Appl. Phys. Lett.* **110**, 191901 (2017).
- [7] D. B. Conkey, A. M. Caravaca-Aguirre, J. D. Dove, H. Ju, T. W. Murray, and R. Piestun, Super-resolution photoacoustic imaging through a scattering wall, *Nat. Commun.* **6**, 7902 (2015).
- [8] Y. Bi, H. Jia, Z. Sun, Y. Yang, H. Zhao, and J. Yang, Experimental demonstration of three-dimensional broadband underwater acoustic carpet cloak, *Appl. Phys. Lett.* **112**, 223502 (2018).
- [9] Y. Chen, X. Liu, and G. Hu, Influences of imperfectness and inner constraints on an acoustic cloak with unidirectional pentamode materials, *J. Sound Vib.* **458**, 62 (2019).
- [10] W. Kan, V. M. García-Chocano, F. Cervera, B. Liang, X.-y. Zou, L.-l. Yin, J. Cheng, and J. Sánchez-Dehesa, Broadband acoustic cloaking within an arbitrary hard cavity, *Phys. Rev. Appl.* **3**, 064019 (2015).
- [11] Z. Sun, X. Sun, H. Jia, Y. Bi, and J. Yang, Quasi-isotropic underwater acoustic carpet cloak based on latticed pentamode metafluid, *Appl. Phys. Lett.* **114**, 094101 (2019).
- [12] J. He, X. Jiang, H. Zhao, C. Zhang, Y. Zheng, C. Liu, and D. Ta, Broadband three-dimensional focusing for an ultrasound scalpel at megahertz frequencies, *Phys. Rev. Appl.* **16**, 024006 (2021).
- [13] Y. Ruan, X. Liang, Z. Wang, T. Wang, Y. Deng, F. Qu, and J. Zhang, 3-D underwater acoustic wave focusing by periodic structure, *Appl. Phys. Lett.* **114**, 081908 (2019).
- [14] L. Fan and J. Mei, Flow-permeable and tunable metalens for subdiffraction waterborne-sound focusing, *Phys. Rev. Appl.* **19**, 024026 (2023).
- [15] H. Peng and J. Mei, High-efficiency and large-numerical-aperture focusing with subdiffraction resolution using a hybrid elastic metalens, *Phys. Rev. Appl.* **21**, 034007 (2024).
- [16] T. Lee, T. Nomura, P. Schmalenberg, E. M. Dede, and H. Iizuka, Directional acoustic superscattering by coupled resonators, *Phys. Rev. Appl.* **12**, 054059 (2019).
- [17] F. Liu, S. Zhang, L. Luo, W. Li, Z. Wang, and M. Ke, Superscattering of sound by a deep-subwavelength solid maze-like rod, *Phys. Rev. Appl.* **12**, 064063 (2019).
- [18] W. Miao, Z. Linghu, Q. Du, P. Peng, and F. Liu, Superscattering of underwater sound via deep learning approach, *Chin. Phys. Lett.* **40**, 014301 (2023).
- [19] M. Landi, J. Zhao, W. E. Prather, Y. Wu, and L. Zhang, Acoustic Purcell effect for enhanced emission, *Phys. Rev. Lett.* **120**, 114301 (2018).
- [20] X. Su and D. Banerjee, Extraordinary sound isolation using an ultrasparse array of degenerate anisotropic scatterers, *Phys. Rev. Appl.* **13**, 064047 (2020).
- [21] X. Zhu, B. Liang, W. Kan, Y. Peng, and J. Cheng, Deep-subwavelength-scale directional sensing based on highly localized dipolar Mie resonances, *Phys. Rev. Appl.* **5**, 054015 (2016).
- [22] V. I. Shcherbinin, V. I. Fesenko, T. I. Tkachova, and V. R. Tuz, Superscattering from subwavelength corrugated cylinders, *Phys. Rev. Appl.* **13**, 024081 (2020).
- [23] H.-W. Wu, Y. Fang, J.-Q. Quan, Y.-Z. Han, Y.-Q. Yin, Y. Li, and Z.-Q. Sheng, Multifrequency superscattering with high Q factors from a deep-subwavelength spoof plasmonic structure, *Phys. Rev. B* **100**, 235443 (2019).
- [24] C. Qian, X. Lin, Y. Yang, X. Xiong, H. Wang, E. Li, I. Kaminer, B. Zhang, and H. Chen, Experimental observation of superscattering, *Phys. Rev. Lett.* **122**, 063901 (2019).
- [25] Z. Qin, C. Qian, L. Shen, X. Wang, I. Kaminer, H. Chen, and H. Wang, Superscattering of water waves, *Natl. Sci. Rev.* **10**, nwac255 (2023).
- [26] S. H. Raad, C. J. Zapata-Rodríguez, and Z. Atlasbaf, Graphene-coated resonators with frequency-selective super-scattering and super-cloaking, *J. Phys. D: Appl. Phys.* **52**, 495101 (2019).
- [27] Z. Ruan and S. Fan, Superscattering of light from subwavelength nanostructures, *Phys. Rev. Lett.* **105**, 013901 (2010).
- [28] Z. Ruan and S. Fan, Design of subwavelength superscattering nanospheres, *Appl. Phys. Lett.* **98**, 043101 (2011).
- [29] Y. Cheng, C. Zhou, B. G. Yuan, D. J. Wu, Q. Wei, and X. J. Liu, Ultra-sparse metasurface for high reflection of low-frequency sound based on artificial Mie resonances, *Nat. Mater.* **14**, 1013 (2015).
- [30] Y. Li, B. Liang, X.-Y. Zou, and J.-C. Cheng, Broadband acoustic transmission enhancement through a structured stiff plate with locally resonant elements, *Chin. Phys. Lett.* **29**, 114301 (2012).
- [31] G. Ma and P. Sheng, Acoustic metamaterials: From local resonances to broad horizons, *Sci. Adv.* **2**, e1501595 (2016).
- [32] W.-J. Sun, H.-W. Wu, P. Hu, N. Zhou, X. Chen, Y.-Q. Yang, and Z.-Q. Sheng, Localized manipulation of spoof surface acoustic skyrmions with deep-subwavelength gradient structures, *Appl. Phys. Lett.* **122**, 202201 (2023).
- [33] G. Zhou, J. H. Wu, K. Lu, X. Tian, W. Huang, and K. Zhu, Broadband low-frequency membrane-type acoustic metamaterials with multi-state anti-resonances, *Appl. Acoust.* **159**, 107078 (2020).
- [34] A. Canós Valero, H. K. Shamkhi, A. S. Kupriianov, T. Weiss, A. A. Pavlov, D. Redka, V. Bobrovs, Y. Kivshar, and A. S. Shalin, Superscattering emerging from the physics of bound states in the continuum, *Nat. Commun.* **14**, 4689 (2023).
- [35] S. Hayati Raad, C. J. Zapata-Rodríguez, and Z. Atlasbaf, Multi-frequency super-scattering from sub-wavelength graphene-coated nanotubes, *J. Opt. Soc. Am. B* **36**, 2292 (2019).

- [36] A. Mirzaei, A. E. Miroschnichenko, I. V. Shadrivov, and Y. S. Kivshar, Superscattering of light optimized by a genetic algorithm, *Appl. Phys. Lett.* **105**, 011109 (2014).
- [37] J. Morris, W. Wang, T. Plaisted, C. J. Hansen, and A. V. Amirkhizi, Optimizing graded metamaterials via genetic algorithm to control energy transmission, *Int. J. Mech. Sci.* **263**, 108775 (2023).
- [38] B. Wu, S. Xue, Z. Zhang, and H. Chen, Invisible devices with natural materials designed by evolutionary optimization, *Phys. Rev. E* **106**, 055312 (2022).
- [39] H. Gao, Z. Gu, S. Liang, T. Liu, J. Zhu, and Z. Su, Enhancing ultrasound transmission and focusing through a stiff plate with inversely optimized auxiliary meta-lens, *Appl. Phys. Lett.* **120**, 111701 (2022).
- [40] L. Fan and J. Mei, Metagratings for waterborne sound: Various functionalities enabled by an efficient inverse-design approach, *Phys. Rev. Appl.* **14**, 044003 (2020).
- [41] H. Meng, J. Wen, H. Zhao, and X. Wen, Optimization of locally resonant acoustic metamaterials on underwater sound absorption characteristics, *J. Sound Vib.* **331**, 4406 (2012).
- [42] See the Supplemental Material at <http://link.aps.org/supplemental/10.1103/PhysRevApplied.21.064011> for more details of the genetic optimization.